AGU ADVANCING EARTH AND SPACE SCIENCE

JGR Solid Earth

RESEARCH ARTICLE

10.1029/2020JB021266

Key Points:

- We develop a theory of wave propagation in infinituple-porosity media based on multiple-scale inclusions
- We consider different distributions of the size of the inclusions aimed to model the anelasticity
- The model provides a reasonable explanation of broadband laboratory and field data

Correspondence to:

J. Ba,
jingba@188.com.

Citation:

Zhang, L., Ba, J., & Carcione, J. M. (2021). Wave propagation in infinituple-porosity media. *Journal of Geophysical Research: Solid Earth*, *126*, e2020JB021266. https://doi.org/10.1029/2020JB021266

Received 30 OCT 2020
Accepted 15 FEB 2021

Wave Propagation in Infinituple-Porosity Media

Lin Zhang[1], Jing Ba[1], and José M. Carcione[2]

[1]School of Earth Sciences and Engineering, Hohai University, Nanjing, China, [2]National Institute of Oceanography and Applied Geophysics – OGS, Trieste, Italy

Abstract The fractal texture (or fabric) of porous media, which supports fluid flow at different scales, is the main cause of wave anelasticity (dispersion and attenuation) on a wide range of frequencies. To model this phenomenon, we develop a theory of wave propagation in a fluid saturated infinituple-porosity media containing inclusions at multiple scales, based on the differential effective medium (DEM) theory of solid composites and Biot-Rayleigh theory for double-porosity media. The dynamical equations are derived from first principles, that is, based on the strain (potential), kinetic, and dissipation energies, leading to generalized stiffness and density coefficients. The scale of the inclusions can be characterized by different distributions. The theory shows that the anelasticity depends on the size (radius) of the inclusions, parameter θ (exponential distribution), mean radius r_0 and variance σ_r^2 (Gaussian distribution) and the fractal dimension D_f (self-similar distribution). When $D_f = 2$, $\theta = 1$ and $\sigma_r^2 = 4$, the three distributions give the same P-wave velocities and attenuation, since each added inclusion phase has nearly the same volume fraction. For the modeling results, the range of anelasticity of $D_f = 2.99/\theta = 1/\sigma_r^2 = 4$ is broader than that of $D_f < 2.99/\theta < 1/\sigma_r^2 < 4$. To confirm the validity of the model, we compare the results with laboratory measurements on tight sandstone and carbonate samples in the range 1 Hz–1 kHz, Fox Hill sandstone (5 Hz–800 kHz) and field measurements of marine sediments (50 Hz–400 kHz). This comparison shows that the model successfully describes the observed anelasticity.

1. Introduction

It is essential in seismic wave propagation in rocks to describe the anelastic behavior observed in a broad range of frequencies to be able to predict their microstructural properties. In particular, this behavior is affected by the rock texture (or fabric) at different scales, which implies fluid flow under the passage of a compressional wave (Borgomano et al., 2017; Zhang et al., 2020). Previous experimental and theoretical evidence shows that the frequency-dependent elastic properties are related to wave-induced fluid flow (WIFF) mechanisms (Ba et al., 2011, 2017; Batzle et al., 2006; Best et al., 2013; Carcione & Picotti, 2006; Guo & Gurevich, 2020a, 2020b; King & Marsden, 2002; Müller et al., 2010; Pimienta et al., 2015a, 2015b; Tisato & Quintal, 2013; Yin et al., 2017, 2019).

Wave propagation is affected by rock microstructure at different scales (Matonti et al., 2015), and effective medium theories can provide reliable models (Benveniste, 1987; David & Zimmerman, 2011; Eshelby, 1957; Jakobsen et al., 2003; Kuster & Toksöz, 1974; Mori & Tanaka, 1973; Norris, 1985; Walsh, 1965; Wu, 1966). Among these models, two of the most popular approaches are differential effective medium (DEM) (Berryman, 1992; Zimmerman, 1991) and self-consistent approximation (SCA) theories (Berryman 1980a, 1980b; Carcione et al., 2020), since both theories take into account the pore and crack interactions. It has been generally accepted that there is no velocity dispersion in dry rocks (Gist, 1994), i.e., their properties are independent of frequency. However, Bailly et al. (2019) found that P-wave velocity of dry rocks decreases from ultrasonic to seismic frequencies, and the phenomenon may be attributed to different microstructural features, such as pores, cracks, and fractures. These authors considered these features at different scales embedded in a host medium, based on a DEM theory, and compared results with measured P-wave velocities.

By considering that the WIFF occurs at the wavelength scale (i.e., the global flow), Biot (1962) derived the equations of elastic wave propagation in a porous medium saturated with a viscous fluid, starting from first principles. He predicted a slow compressional wave, caused by the differential motion between the skeleton and the pore fluid (Biot, 1956). At low frequencies, this motion can be neglected and the P-wave velocity is consistent with Gassmann equation (Gassmann, 1951). However, Biot theory underestimates the wave dispersion and attenuation observed in laboratory and field experiments. WIFF occurs at microscopic and mesoscopic scales, at the pore scale and heterogeneities much smaller than the wavelength, respectively. The microscopic mechanisms involve fluid flow between stiff pores and compliant cracks (squirt flow) (Chapman et al., 2002; Gurevich et al., 2010; Mavko & Jizba, 1991; Mavko & Nur, 1975). The global and squirt flow mechanisms exist simultaneously in a cracked porous medium and a number of theoretical models have been developed (Carcione & Gurevich, 2011; Dvorkin & Nur, 1993; Tang, 2011; Tang et al., 2012; Wu et al., 2020; Yao et al., 2015; Zhang, Ba, et al., 2019).

On the other hand, WIFF at the mesoscopic scale (larger than the grain scale but much smaller than the wavelength), occurs in patchy saturated media or when the flow occurs between the two constituents of different frame compressibility. This WIFF occurs in a wide range of scales. The effect of this mechanism on wave dispersion and attenuation have been investigated by the researchers (Ba et al, 2011, 2012; Carcione et al., 2003; Liu et al., 2009, 2010; Pride et al., 2004; Santos et al., 2015; White, 1975; White et al., 1975; Zheng et al., 2017), and it is considered that this mechanism is capable of describing wave attenuation in the seismic exploration band. However, these models assumed single-scale fluid flow. By considering two mesoscopic flow mechanisms induced by rock fabric and patchy saturation, Ba et al. (2015, 2017) developed a double double-porosity model. Based on Ba et al. (2015), Sun et al. (2016) considered a triple-layer spherical patch, where the size of the fluid pocket can be larger or smaller than the size of the solid inclusion. This model was extended to an ellipsoidal triple-layer patch containing flat pore spaces and penny-shaped cracks (Sun et al., 2018).

Zhang, Yang, et al. (2019) proposed a model to analyze the effects of WIFF at the microscopic and mesoscopic scales on wave dispersion and attenuation. By considering that local fluid flow occurs at different scales, Sun and Gurevich (2020) developed a model by combining the stress-dependent (David & Zimmerman, 2012) and squirt-flow models (Glubokovskikh et al., 2016; Gurevich et al., 2010). Similarly, Zhao et al. (2020) investigated the effect of pore pressure caused by elastic interactions between ellipsoidal pores on the elastic properties. All these theoretical models assume a given shape or size of the fabric structures and cannot fully characterize the effect of WIFF on wave propagation at different scales. In fact, the fabric geometrical features are inherently complex, and some studies considered a random distribution characterized by autocorrelation functions, such as the exponential and Gaussian ones (Ikelle et al., 1993; Klimeš, 2002; Rao et al., 2020). Following this approach, Pride and Masson (2006), Müller and Gurevich (2005), and Müller et al. (2008) studied the effects of fluid patches on wave attenuation. Furthermore, other experimental studies indicated that the fabric distribution is self-similar or fractal (Katz & Thompson, 1985; Krohn, 1988).

The motivation of this study is to establish the relation between wave anelasticity and fabric heterogeneity by assuming that the inclusions are scale-dependent. We develop an infinituple-porosity media (IPM) model, based on the DEM and Biot-Rayleigh theories (Section 2). By considering that the inclusions are characterized by exponential, Gaussian and self-similar distributions, we provide numerical examples to analyze the effect of different distributions on wave dispersion and attenuation (Section 3). The theoretical results are compared with the broadband measurements in the laboratory and with field data (Section 4). Then, Section 5 discusses the influence of how the inclusions are added and the reliability of the results. Finally, conclusions are presented in Section 6.

2. Energies and Wave Propagation

We assume that the inclusions (1) are spherical, (2) have different dry-rock bulk and shear moduli, ${K_{bI}}^m$ and ${G_{bI}}^m$, (3) have a dilute concentration to avoid mutual interactions, (4) have different matrix porosity, ϕ_{Im}, (5) have different permeability, ${\kappa_I}^m$ and (6) have different radius, r_m. The total porosity is $\phi = \phi_{00}v_0 + \phi_{I1}v_1 + \cdots + \phi_{Im}v_m + \cdots$, where v_m is the volume fraction of the m-th inclusion phase, ϕ_{00} and v_0 are the matrix porosity and volume fraction of the initial host medium, respectively.

2.1. Strain (Potential), Kinetic and Dissipation Energies

In this section, we describe a procedure whereby the IPM model can be realized. In the first addition, the inclusion phase with volume fraction v_1 is embedded into an initial host medium with volume fraction v_0.

Then, the volume fractions of the host medium and inclusions in the new medium are $v_{1,H} = v_0 / \left(v_0 + v_1\right)$ and $v_{1,I} = v_1/(v_0+v_1)$, respectively, the corresponding absolute porosities are $\phi_{1,H} = \phi_{00} v_{1,H}$ and $\phi_{1,I} = \phi_{I1} v_{1,I}$, and the total porosity is $\phi_{1,T} = \phi_{1,H} + \phi_{1,I}$. In a similar way, the volume fractions of the two components in a new medium after the m-th addition are $v_{m,H} = \left(v_0 + v_1 + \cdots + v_{m-1}\right) / \left(v_0 + v_1 + \cdots + v_m\right)$ and $v_{m,I} = v_m / \left(v_0 + v_1 + \cdots + v_m\right)$, respectively. The corresponding absolute porosities are $\phi_{m,H} = \phi_{m-1,T} v_{m,H}$ and $\phi_{m,I} = \phi_{Im} v_{m,I}$, and the total porosity is $\phi_{m,T} = \phi_{m,H} + \phi_{m,I}$. Note that the matrix porosity of the host medium is the total porosity from the previous addition.

At each addition, the new medium can be treated as a double-porosity medium. To simplify the equations, the porosity ($\phi_{m,H}$) and matrix porosity ($\phi_{m-1,T}$) of the host medium can be denoted with ϕ and ϕ_{H0}, respectively. Because the fabric is represented by inclusions, their volume fraction v_m is dimensionless. Then, the incremental porosity is also dimensionless, the porosity $\phi_{m,I}$ is expressed as $d\phi$. Similarly, the matrix porosity (ϕ_{Im}), the dry-rock bulk modulus ($K_{bI}{}^{m}$) and permeability ($\kappa_I{}^{m}$) of the inclusions are expressed as ϕ_{I0}, K_{bI}, and κ_I, respectively.

By considering that the rock fabric has a broad size distribution, we develop an IPM model based on the DEM theory of solid composites (e.g., Berryman, 1992), where the fabric is treated as inclusions of different sizes and physical properties. The inclusions are added incrementally into a homogeneous host medium (see Figure 1). Each addition is composed of a set of inclusions with the same physical properties and radius. Then, a new double-porosity medium is built and the equivalent response of the host medium plus inclusions is obtained with the Biot-Rayleigh theory (Ba et al., 2011). This equivalent homogeneous medium is considered as the host medium in the next addition of inclusions. According to Ba at al. (2011), the strain energy of a double-porosity medium is

$$2W = \left(\tilde{A} + 2\tilde{N}\right) I_1^2 - 4\tilde{N} I_2 + 2\tilde{Q}_H I_1 \left(\xi_H + \zeta d\phi\right) + \tilde{R}_H \left(\xi_H + \zeta d\phi\right)^2 + 2\tilde{Q}_I I_1 \left(\xi_I - \phi\zeta\right) + \tilde{R}_I \left(\xi_I - \phi\zeta\right)^2, \quad (1)$$

where I_1, I_2, I_3 are the three rotation invariants of the matrix (frame) and ξ_H and ξ_I are the fluid strains in the host medium and inclusions, respectively. The scalar ζ denotes the fluid strain increment between the host and inclusions with radius r_0 ($r_0 = r_m$), given by

$$\zeta = \frac{1}{\phi}\left(1 - \frac{r_0^3}{r^3}\right), \quad (2)$$

where r is the dynamic radius of the inclusion after WIFF, and the Biot stiffness coefficients are

$$\tilde{A} = \left(1 - \phi - d\phi\right) K_s - \frac{2}{3}\tilde{N} - \tilde{Q}_H K_s / K_f - \tilde{Q}_I \left(K_s \phi\right) / \left(K_f d\phi\right) \quad (3a)$$

$$\tilde{N} = G_b, \quad (3b)$$

$$\tilde{Q}_H = \frac{\beta\phi\left(1 - \phi - d\phi - K_b / K_s\right) K_s}{\beta\left(1 - \phi - d\phi - K_b / K_s\right) + K_s / K_f \left(\beta\phi + d\phi\right)}, \quad (3c)$$

$$\tilde{Q}_I = \frac{\left(1 - \phi - d\phi - K_b / K_s\right)\phi K_s}{1 - \phi - d\phi - K_b / K_s + K_s / K_f \left(\beta\phi + d\phi\right)}, \quad (3d)$$

$$\tilde{R}_H = \frac{\left(\beta\phi + d\phi\right)\phi K_s}{\beta\left(1 - \phi - d\phi - K_b / K_s\right) + K_s / K_f \left(\beta\phi + d\phi\right)}, \quad (3e)$$

$$\tilde{R}_I = \frac{\left(\beta\phi + d\phi\right) K_s d\phi}{1 - \phi - d\phi - K_b / K_s + K_s / K_f \left(\beta\phi + d\phi\right)}, \quad (3f)$$

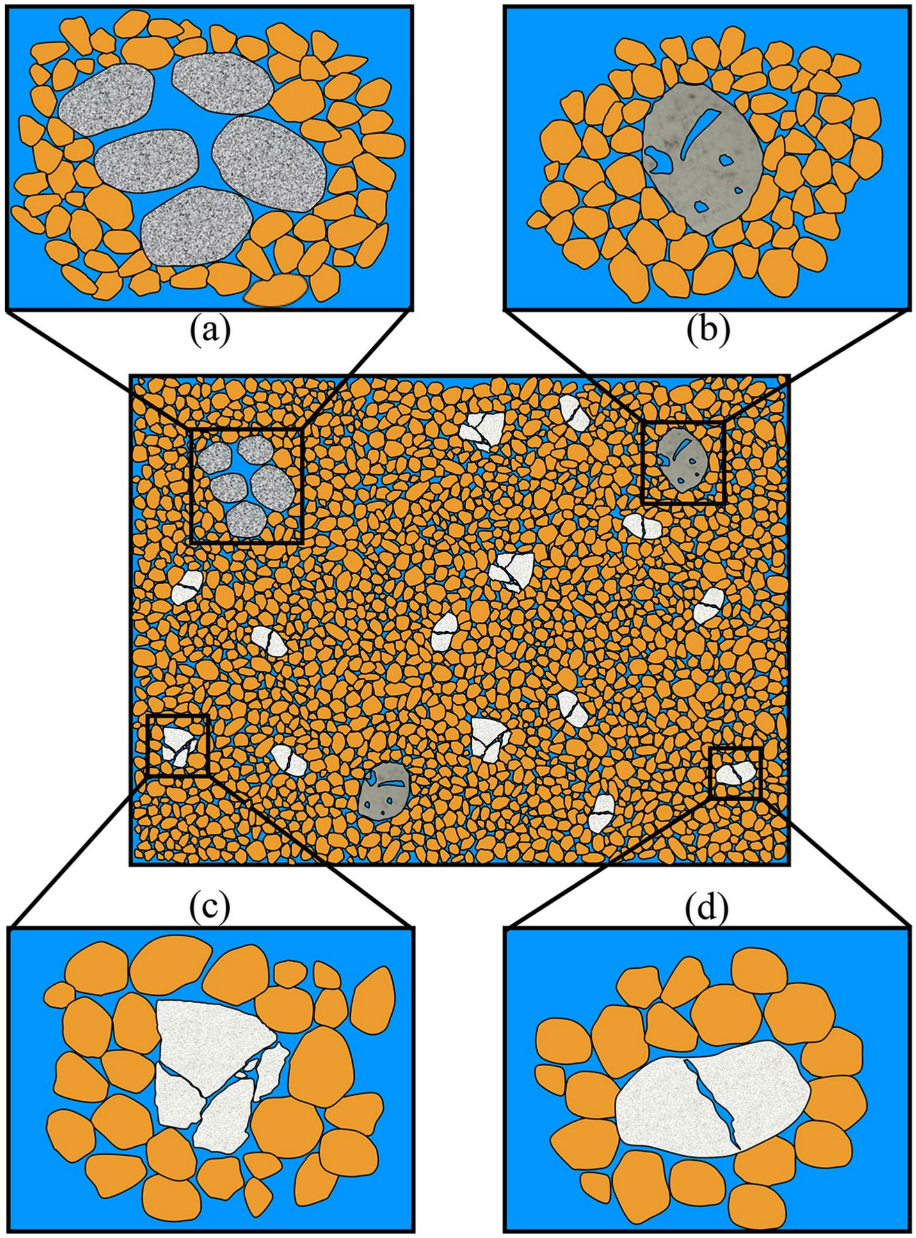

Figure 1. Idealized illustration of fabric structures, where different types of inclusions are embedded into a host skeleton (a) Uncemented or loose-contact granular material. (b) Large grains with dissolved pores. (c) Grain aggregates with defined contacts. (d) Grains with intragranular microcracks.

$$\beta = \frac{\phi_{I0}}{\phi_{H0}}\left[\frac{1-\left(1-\phi_{H0}\right)K_s \;/\; K_{bH}}{1-\left(1-\phi_{I0}\right)K_s \;/\; K_{bI}}\right], \tag{3g}$$

where K_s (K_f) is the grain (fluid) bulk modulus, K_{bH} (G_{bH}) is the dry-rock bulk (shear) modulus of the initial host medium, and K_b and G_b are the dry-composite bulk and shear moduli, respectively, which are given by the differential scheme (Berryman, 1992).

The kinetic energy function T for a double-porosity medium is (Ba et al., 2011; Biot, 1962)

$$2T = \tilde{\rho}_{00}\sum_i \dot{u}_i^2 + 2\tilde{\rho}_{01}\sum_i \dot{u}_i\dot{U}_{i,H} + 2\tilde{\rho}_{02}\sum_i \dot{u}_i\dot{U}_{i,I} + \tilde{\rho}_{11}\sum_i \dot{U}_{i,H}^2 + \tilde{\rho}_{22}\sum_i \dot{U}_{i,I}^2 + 2T_{LFF}, \tag{4}$$

where $\mathbf{u} = [u_1, u_2, u_3]$, $\mathbf{U}_H = [U_{1,H}, U_{2,H}, U_{3,H}]$ and $\mathbf{U}_I = [U_{1,I}, U_{2,I}, U_{3,I}]$ are the solid displacement, and fluid displacements in the host medium and inclusions, respectively. T_{LFF} is the kinetic energy function induced by the WIFF between the inclusions and host medium,

$$T_{LFF} = \frac{1}{6}\left(\frac{\phi^2 \phi_{I0} d\phi}{\phi_{H0}}\right)\rho_f r_0^2 \dot{\zeta}^2. \tag{5}$$

The density coefficients are

$$\tilde{\rho}_{00} = (1 - \phi - d\phi)\rho_s - \tilde{\rho}_{01} - \tilde{\rho}_{02}, \tag{6a}$$

$$\tilde{\rho}_{01} = \phi\rho_f - \tilde{\rho}_{11}, \tag{6b}$$

$$\tilde{\rho}_{02} = \rho_f d\phi - \tilde{\rho}_{22}, \tag{6c}$$

$$\tilde{\rho}_{11} = \alpha_H \phi \rho_f, \tag{6d}$$

$$\tilde{\rho}_{22} = \alpha_I \rho_f d\phi, \tag{6e}$$

where ρ_s (ρ_f) is the grain (fluid) density, and α_H and α_I are the tortuosities of the host and inclusions, respectively, which are given by Berryman (1979)

$$\alpha_H = \frac{1}{2}\left(1 + \frac{1}{\phi_{H0}}\right) \text{ and } \alpha_I = \frac{1}{2}\left(1 + \frac{1}{\phi_{I0}}\right). \tag{7}$$

Similarly, the dissipation function of a double-porosity medium is

$$2D = \tilde{b}_1\left(\dot{\mathbf{u}} - \dot{\mathbf{U}}_H\right)\left(\dot{\mathbf{u}} - \dot{\mathbf{U}}_H\right) + \tilde{b}_2\left(\dot{\mathbf{u}} - \dot{\mathbf{U}}_I\right)\left(\dot{\mathbf{u}} - \dot{\mathbf{U}}_I\right) + 2D_{LFF}, \tag{8}$$

where

$$D_{LFF} = \frac{1}{6}\frac{\eta}{\kappa_H}\phi^2\phi_{I0} r_0^2 \dot{\zeta}^2 d\phi, \tag{9}$$

is the dissipation energy function induced by the WIFF between the inclusions and host medium, η is the fluid viscosity, κ_H is the permeability of the host medium, and

$$\tilde{b}_1 = \frac{\phi\phi_{H0}\eta}{\kappa_H}, \tag{10a}$$

$$\tilde{b}_2 = \frac{\phi_{I0}\eta d\phi}{\kappa_I}. \tag{10b}$$

2.2. Wave Propagation Equations

Using Hamilton's principle and the Lagrangian equation $L = T\text{-}W$, we obtain the dynamical equations

$$\begin{aligned}&\tilde{N}\nabla^2\mathbf{u} + \left(\tilde{A} + \tilde{N}\right)\nabla e + \tilde{Q}_H \nabla\left(\xi_H + \zeta d\phi\right) + \tilde{Q}_I \nabla\left(\xi_I - \phi\zeta\right) \\ &\quad = \tilde{\rho}_{00}\ddot{\mathbf{u}} + \tilde{\rho}_{01}\ddot{\mathbf{u}}_H + \tilde{\rho}_{02}\ddot{\mathbf{u}}_I + \tilde{b}_1\left(\dot{\mathbf{u}} - \dot{\mathbf{U}}_H\right) + \tilde{b}_2\left(\dot{\mathbf{u}} - \dot{\mathbf{U}}_I\right),\end{aligned} \tag{11a}$$

$$\tilde{Q}_H \nabla e + \tilde{R}_H \nabla\left(\xi_H + \zeta d\phi\right) = \tilde{\rho}_{01}\ddot{\mathbf{u}} + \tilde{\rho}_{11}\ddot{\mathbf{u}}_H - \tilde{b}_1\left(\dot{\mathbf{u}} - \dot{\mathbf{U}}_H\right), \tag{11b}$$

$$\tilde{Q}_I\nabla e + \tilde{R}_I\nabla\left(\xi_I - \phi\zeta\right) = \tilde{\rho}_{02}\ddot{\mathbf{u}} + \tilde{\rho}_{22}\ddot{\mathbf{u}}_I - \tilde{b}_2\left(\dot{\mathbf{u}} - \dot{\mathbf{U}}_I\right), \tag{11c}$$

$$\left(\tilde{Q}_H\nabla e + \tilde{R}_H\nabla\left(\xi_H + \zeta d\phi\right)\right)d\phi - \phi\left(\tilde{Q}_I\nabla e + \tilde{R}_I\nabla\left(\xi_I - \phi\zeta\right)\right) = \frac{1}{3}r_0^2\phi^2\phi_{I0}d\phi\left(\frac{\rho_f}{\phi_{H0}}\ddot{\zeta} + \frac{\eta}{\kappa_H}\dot{\zeta}\right), \tag{11d}$$

where e is the solid divergence field. The stiffness, density and dissipation coefficients in Equations 3, 6 and 10 are also a function of ϕ and $d\phi$. Hence, there are high-order terms in $d\phi$ in Equation 11. Let us define

$$B_1 = \left(\beta\left(1 - \phi - K_b / K_s\right) + K_s / K_f\beta\phi\right) + \left(-\beta + K_s / K_f\right)d\phi \tag{12a}$$

$$B_2 = \left(\left(1 - \phi - K_b / K_s\right) + K_s / K_f\beta\phi\right) + \left(-1 + K_s / K_f\right)d\phi. \tag{12b}$$

and multiply Equations 11a and 11d by B_1B_2, Equation 11b by B_1 and Equation 11c by B_2. Neglecting high-order terms in $d\phi$, we obtain

$$\begin{aligned}\left(N + NSd\phi\right)\nabla^2\mathbf{u} + \left(A + N\right)\nabla e + \left(A_d + NS\right)d\phi\nabla e + Q_H\phi\nabla\left(\xi_H + \zeta d\phi\right) + R_H\left(\frac{Q_I}{K_f} - \frac{Q_I}{K_s} - 1\right)\\ d\phi\nabla\xi_H + Q_Id\phi\nabla\left(\xi_I - \phi\zeta\right) = \rho_{00}\ddot{\mathbf{u}} + \left(\rho_{00}S - \rho_s - \rho_{02}\right)d\phi\ddot{\mathbf{u}} + \rho_{01}\phi\ddot{\mathbf{u}}_H + \rho_{01}\phi Sd\phi\ddot{\mathbf{u}}_H\\ +\rho_{02}d\phi\ddot{\mathbf{u}}_I + \frac{\phi\phi_{H0}\eta}{\kappa_H}\left(\dot{\mathbf{u}} - \dot{\mathbf{U}}_H\right) + \frac{\phi\phi_{H0}\eta}{\kappa_H}Sd\phi\left(\dot{\mathbf{u}} - \dot{\mathbf{U}}_H\right) + \frac{\phi_{I0}\eta d\phi}{\kappa_I}\left(\dot{\mathbf{u}} - \dot{\mathbf{U}}_I\right),\end{aligned} \tag{13a}$$

$$\begin{aligned}Q_H\nabla e + R_H\nabla\left(\xi_H + \zeta d\phi\right) + \frac{R_H}{\phi}\left(\frac{1}{\beta}\nabla\xi_H - \nabla e\right)d\phi\\ = \left(1 + \frac{R_H}{\phi}\left(\frac{1}{\beta K_f} - \frac{1}{K_s}\right)d\phi\right)\left(\rho_{01}\ddot{\mathbf{u}} + \rho_{11}\ddot{\mathbf{U}}_H - \frac{\phi_{H0}\eta}{\kappa_H}\left(\dot{\mathbf{u}} - \dot{\mathbf{U}}_H\right)\right),\end{aligned} \tag{13b}$$

$$Q_I\nabla e + R_I\nabla\left(\xi_I - \phi\zeta\right) = \rho_{02}\ddot{\mathbf{u}} + \rho_{22}\ddot{\mathbf{u}}_I - \frac{\phi_{I0}\eta}{\kappa_I}\left(\dot{\mathbf{u}} - \dot{\mathbf{U}}_I\right), \tag{13c}$$

$$\left(Q_He + R_H\left(\xi_H + \zeta d\phi\right)\right) - \left(Q_Ie + R_I\left(\xi_I - \phi\zeta\right)\right) = \frac{1}{3}r_0^2\phi\phi_{I0}\left(\frac{\rho_f}{\phi_{H0}}\ddot{\zeta} + \frac{\eta}{\kappa_H}\dot{\zeta}\right), \tag{13d}$$

where

$$A = \left(1 - \phi\right)K_s - \frac{2}{3}N - K_s / K_fQ_H\phi, \tag{14a}$$

$$A_d = \left(1 - \phi\right)K_sS - \frac{2}{3}NS - Q_IR_H\left(K_s / K_f^2 - 1 / K_f\right) - \left(Q_I - R_H\right)K_s / K_f - K_s, \tag{14b}$$

$$N = \tilde{N}, \tag{14c}$$

$$Q_H = \frac{K_s\left(1 - \phi - K_b / K_s\right)}{1 - \phi - K_b / K_s + K_s / K_f\phi}, \tag{14d}$$

$$Q_I = \frac{K_s\left(1 - \phi - K_b / K_s\right)}{1 - \phi - K_b / K_s + K_s / K_f\beta\phi}, \tag{14e}$$

$$R_H = \frac{K_s\phi}{1 - \phi - K_b / K_s + K_s / K_f\phi}, \tag{14f}$$

$$R_I = \frac{K_s \beta \phi}{1 - \phi - K_b / K_s + K_s / K_f \beta \phi}, \tag{14g}$$

$$S = R_H / \phi \left(1 / \beta / K_f - 1 / K_s\right) + R_I / \beta / \phi \left(1 / K_f - 1 / K_s\right), \tag{14h}$$

$$\rho_{00} = \left(1 - \phi\right) \rho_s - \rho_{01}, \tag{14i}$$

$$\rho_{01} = \left(1 - \alpha_H\right) \rho_f, \tag{14j}$$

$$\rho_{02} = \left(1 - \alpha_I\right) \rho_f, \tag{14k}$$

$$\rho_{11} = \alpha_H \rho_f, \tag{14l}$$

$$\rho_{22} = \alpha_I \rho_f. \tag{14m}$$

Compared with Equations 3 and 6, the stiffness and density coefficients in Equation 14 are dependent on ϕ, and note that first-order terms in $d\phi$ appear in Equation 13.

The P- and S-wave complex wave numbers (k_P and k_S) are obtained with a plane-wave analysis of Equation 13 [see Equations B1–B4 in Ba et al. (2011)]. Then, the complex bulk and shear moduli of the composite porous medium are

$$K_{\text{sat}} = \left(\left(1 - \phi - d\phi\right) \rho_s + \left(\phi + d\phi\right) \rho_f\right) \left(\frac{\omega}{k_P}\right)^2 - \frac{4}{3} G_{\text{sat}}, \tag{15a}$$

$$G_{\text{sat}} = \left(\left(1 - \phi - d\phi\right) \rho_s + \left(\phi + d\phi\right) \rho_f\right) \left(\frac{\omega}{k_S}\right)^2, \tag{15b}$$

where ρ_f is the fluid density and ω is the angular frequency.

Gassmann Equations (Gassmann, 1951) are applied to compute the dry-rock complex moduli at the end of each addition, and used as the dry moduli of the new host medium for the next addition.

$$\frac{K_{\text{sat}}}{K_s - K_{\text{sat}}} = \frac{K_b}{K_s - K_b} + \frac{K_f}{\left(\phi + d\phi\right)\left(K_s - K_f\right)}, \tag{16a}$$

$$G_b = G_{\text{sat}}. \tag{16b}$$

By using Equations 13–16 at each addition, all inclusions are added incrementally until the final IPM is obtained.

2.3. Infinituple-Porosity Theory

The size of the inclusion follows simple correlation functions (Klimeš, 2002), with $d\phi = \phi^{'}(r)dr$. The integral Equations of wave propagation in the IPM are

$$\begin{aligned} &\bar{N}\nabla^2 \mathbf{u} + \left(\bar{A} + \bar{N}\right)\nabla e + \bar{Q}_H \phi \nabla\left(\xi_H + \int_0^\infty \zeta \phi'(r) dr\right) + \int_0^\infty \bar{Q}_I \phi'(r) \nabla\left(\xi_I - \phi\zeta\right) dr \\ &= \bar{\rho}_{00}\ddot{\mathbf{u}} + \bar{\rho}_{01}\phi\ddot{\mathbf{U}}_H + \int_0^\infty \bar{\rho}_{02}\phi'(r)\ddot{\mathbf{U}}_I dr + \frac{\phi\bar{\phi}_{H0}\eta}{\bar{\kappa}_H}\left(\dot{\mathbf{u}} - \dot{\mathbf{U}}_H\right) + \eta\int_0^\infty \frac{\phi_{I0}}{\kappa_I}\left(\dot{\mathbf{u}} - \dot{\mathbf{U}}_I\right)\phi'(r) dr, \end{aligned} \tag{17a}$$

$$\bar{Q}_H \nabla e + \bar{R}_H \nabla\left(\xi_H + \int_0^\infty \phi'(r)\zeta dr\right) = \bar{\rho}_{01}\ddot{\mathbf{u}} + \bar{\rho}_{11}\ddot{\mathbf{U}}_H - \frac{\bar{\phi}_{H0}\eta}{\bar{\kappa}_H}\left(\dot{\mathbf{u}} - \dot{\mathbf{U}}_H\right), \tag{17b}$$

$$\bar{Q}_I \nabla e + \bar{R}_I \nabla \left(\xi_I - \zeta \right) = \bar{\rho}_{02}\, \ddot{\mathbf{u}} + \bar{\rho}_{22} \ddot{\mathbf{U}}_I - \frac{\phi_{I0}\eta}{\kappa_I} \left(\dot{\mathbf{u}} - \dot{\mathbf{U}}_I \right), \tag{17c}$$

$$\left(\bar{Q}_H e + \bar{R}_H \left(\xi_H + \int_0^{\infty} \zeta \phi'(r) dr \right) \right) - \left(\bar{Q}_I e + \bar{R}_I \left(\xi_I - \phi\zeta \right) \right) = \frac{1}{3} r_0^2 \phi \phi_{I0} \left(\frac{\rho_f}{\bar{\phi}_{H0}} \ddot{\zeta} + \frac{\eta}{\bar{\kappa}_H} \dot{\zeta} \right), \tag{17d}$$

where ϕ_{I0} and κ_I correspond to a scale (radius) r. $\bar{\phi}_{H0}$, $\bar{\kappa}_H$, the stiffnesses $\bar{A}$, $\bar{N}$, $\bar{Q}_H$, $\bar{Q}_I$, $\bar{R}_H$ and $\bar{R}_I$, and the density coefficients $\bar{\rho}_{00}$, $\bar{\rho}_{01}$, $\bar{\rho}_{02}$, $\bar{\rho}_{11}$, and $\bar{\rho}_{22}$, are obtained as in the discretization procedure of Section 2.1. In the discretization progress, Equations 13–16 are used in each iteration and the final P and S wave numbers are obtained at the last iteration, which are used to compute the wave velocity and attenuation of the final IPM.

3. Numerical Examples

3.1. Random-Fractal Porous Media

3.1.1. Exponential Distribution

First, we assume that the distribution of inclusions is exponential, so that the volume fractions are (Müller & Gurevich, 2005)

$$v_{I,E} = \frac{1}{\theta} e^{\frac{-r}{\theta}}, \tag{18}$$

with $\theta > 0$ is a constant. We assume that the inclusion radii are distributed in the ranges (0.01–50) and (0.001–50) mm, and the total volume fraction is 0.1. Then, the inclusions are divided into 25 additions and the volume fraction of each addition is determined by Equation 18. The volume fractions of the inclusions as a function of the inclusion radii and different values of θ (10^{-3}, 10^{-2}, 10^{0}) are shown in Figure 2. They decrease exponentially with increasing radius and tend to be the same as the θ increases (see black, blue, and red curves with triangles).

An example is presented here to analyze how the inclusions at multiple scales affect the wave attenuation and dispersion, where the bulk modulus of the grain is 38 GPa and its density is 2,650 kg/m^3. We further assume that the inclusions have the same dry-rock elastic moduli and matrix porosity, with the other properties listed in Table 1. The volume fractions of the inclusions are the same as those of Figure 2. Figure 3 shows the P-wave velocity (V_P) and attenuation ($1/Q$) as a function of frequency for different values of θ and scale ranges. Comparing the black, blue and red curves for the same scale shows that the dispersion and attenuation ranges are wider with increasing θ. Moreover, at the same θ (see brown and black curves), the P-wave velocity decreases as the scale range of the inclusion radii increases, and the difference in the P-wave velocity (and attenuation) is quite pronounced, which indicates that volume fraction of the inclusion phases is significantly different at different scale ranges (see brown and black curves with triangles in Figure 2). It can be seen that the low- and high frequency P-wave velocities tend to the same value when the total inclusion volume fraction is constant.

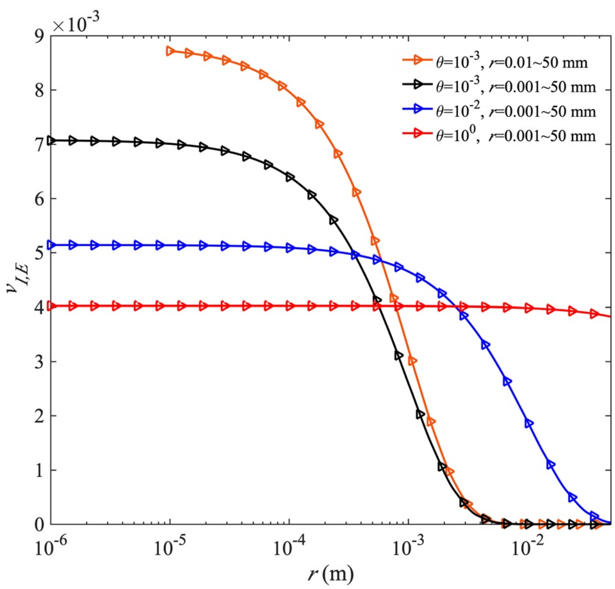

Figure 2. Volume fractions of the inclusion phases as a function of inclusion radius for different values of θ.

3.1.2. Gaussian Distribution

In this case, we consider a mean radius r_0 and variance σ_r^2, and the volume fractions (Müller & Gurevich, 2005; Sarout, 2012)

$$v_{I,G} = \frac{1}{\sqrt{2\pi\sigma_r^2}} \exp\left(-\frac{\left(r - r_0 \right)^2}{2\sigma_r^2} \right) \tag{19}$$

Table 1
Rock Frame and Fluid Properties

K_{bH} (GPa)	G_{bH} (GPa)	K_{bI} (GPa)	G_{bI} (GPa)	ϕ_{H0} (%)	ϕ_{I0} (%)	κ_H D	κ_I D	K_f (GPa)	ρ_f (kg/m^3)	η Pa•s
17	15	1.7	1.5	15	8	0.01	1	2.5	1040	0.001

We assume that the scale (radius) range and total volume fraction are the same as in Section 3.1.1. Figure 4 shows the volume fractions of the inclusions for different mean radius r_0 and variance σ_r^2. When r_0 and the scale range are the same (see black, blue and red curves with triangles), the volume fractions tend to be the same as the variance σ_r^2 increases. In contrast, when σ_r^2 and the scale range are the same (see black and magenta curves with triangles), the curve shifts toward the high inclusion radius end with increasing mean radius r_0.

The P-wave velocity and attenuation as a function of frequency with different mean radius r_0 and variance σ_r^2 are shown in Figure 5, by using the properties listed in Table 1. At the same r_0 and scale range (see black, blue and red curves), the P-wave velocity increases with increasing σ_r^2 in the frequency range 10^0- $\approx 10^5$ Hz, whereas it decreases in the range $\approx 10^5$–10^8 Hz, and the dispersion and attenuation occur over a broader frequency band. Keeping constant σ_r^2 and the scale range (see black and magenta curves), the P-wave velocity curve shifts toward the low frequency end with increasing r_0, indicating that this radius only affects the relaxation frequency of WIFF, and not the degree of anelasticity. With increasing scale range, the dispersion (and attenuation) curves almost overlap in the case of a Gaussian distribution with the same σ_r^2 and r_0 (brown and black curves in Figure 5 in comparison with Figure 3). However, the velocity decrease is much more pronounced in the case of the exponential distribution (brown and black curves in Figure 3a). This is because the difference between volume fractions of the inclusion phases is obvious in the latter (brown and black curves with triangles in Figure 2) compared with the former (brown and black curves with triangles in Figure 4).

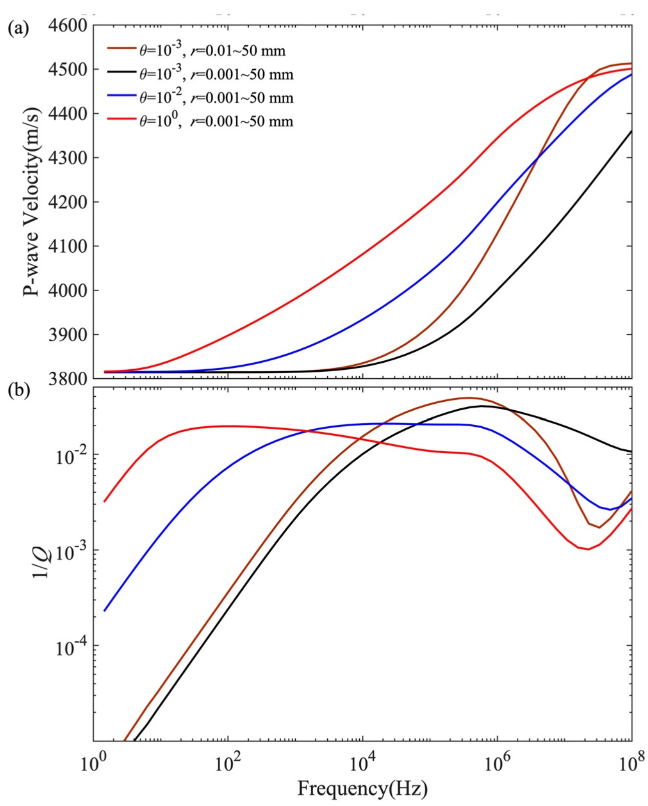

Figure 3. (a) P-wave velocity and (b) $1/Q$ as a function of frequency for different values of θ.

3.2. Comparison With a Self-Similar Medium

In a self-similar rock, the volume fractions are (Rieu & Perrier, 1998)

$$v_{I,F} = 1 - \left(\frac{r_{\min}}{r_{\max}}\right)^{D_E - D_f}, \tag{20}$$

where $r_{\min}$ and $r_{\max}$ are the minimum and maximum inclusion radii, respectively. D_E is the Euclidean dimension, and D_f is the fractal dimension satisfying $2 < D_f < 3$.

A comparison of the results for self-similar, exponential and Gaussian distributions is given in Figure 6, according to the properties of Table 1. The results show that when each added inclusion phase has nearly the same volume fraction, that is, $D_f = 2$, $\theta = 10^0$ and $\sigma_r^2 = 4$, the P-wave velocities and attenuation are almost the same. For the self-similar distribution, the range of anelasticity of $D_f = 2.99$ is broader than that of $D_f < 2.99$. For the exponential distribution, the range of anelasticity of $\theta = 1$ is broader than that of $\theta < 1$. For the Gaussian distribution, the range of anelasticity of $\sigma_r^2 = 4$ is broader than that of $\sigma_r^2 < 4$. The difference in the results is related to the different parameter set (θ, σ_r^2, D_f), while the low- and high-frequency velocities coincide for the three distributions.

10.1029/2020JB021266

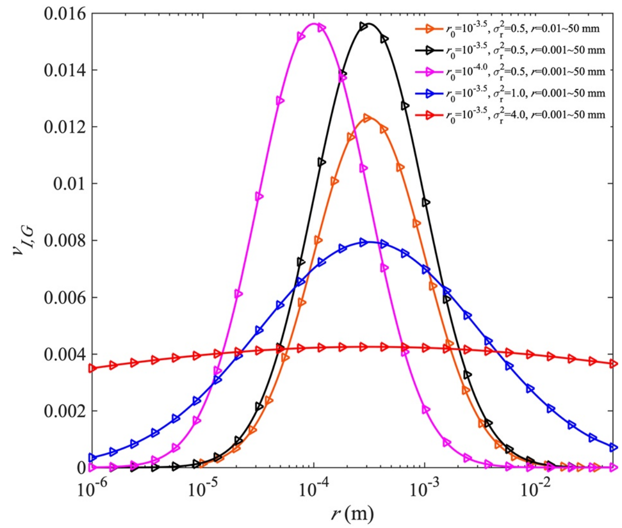

Figure 4. Volume fractions of the inclusion phases as a function of inclusion radius for different mean value of r_0, variance σ_r^2 and scale range.

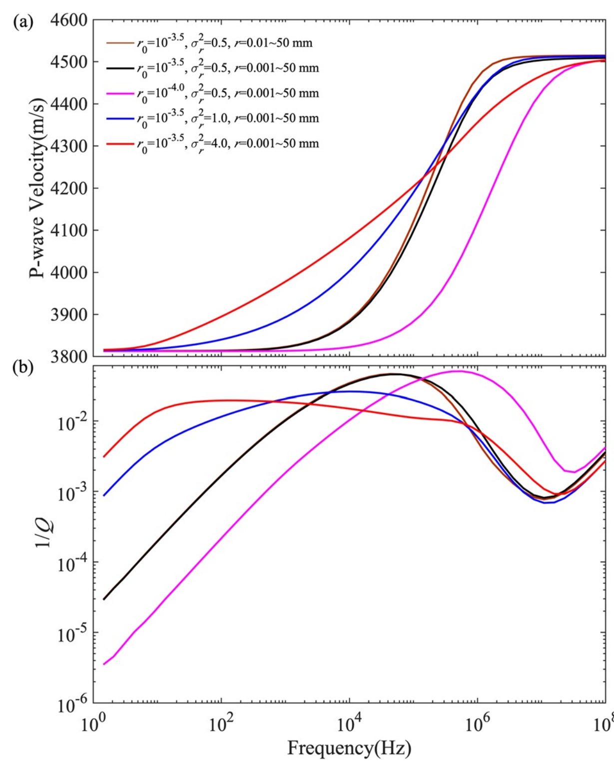

Figure 5. (a) P-wave velocity and (b) $1/Q$ as a function of frequency for different mean value of r_0, variance σ_r^2 and scale range.

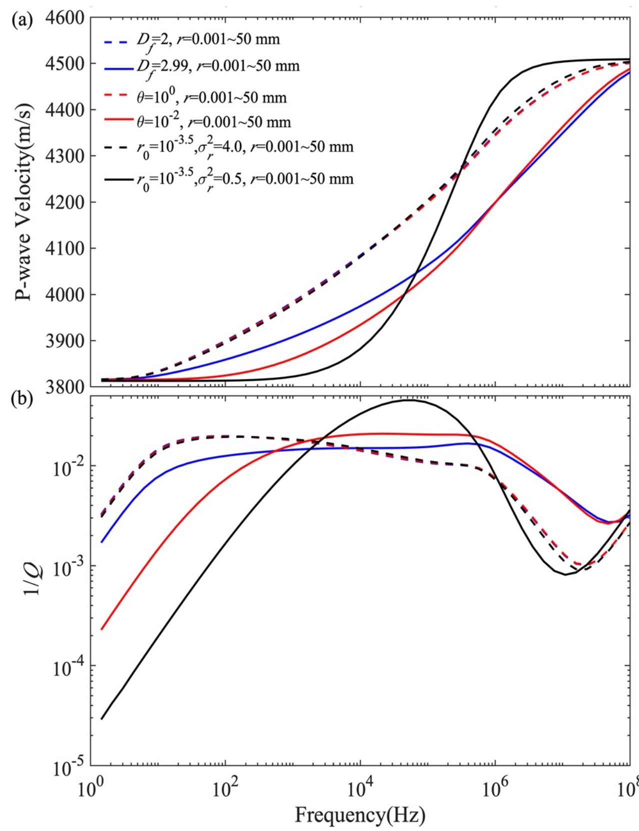

Figure 6. (a) P-wave velocity and (b) 1/Q as a function of frequency for self-similar, exponential and Gaussian distributions of the inclusions. The blue dashed and solid curves represent $D_f = 2$ and 2.99, respectively, the red dashed and solid curves represent $\theta = 10^0$ and 10^{-2}, respectively, and the black dashed and solid curves represent $r_0 = 10^{-3.5}$ and $\sigma_r{}^2 = 4.0$, and $r_0 = 10^{-3.5}$ and $\sigma_r{}^2 = 0.5$, respectively.

4. Examples

4.1. Laboratory Measurements in Tight Rocks

The experimental data of two tight-rock samples reported by Li et al. (2020) are considered to illustrate the proposed theory. Two samples are from the He-8 section of the Ordos reservoirs, where one of them is a tight carbonate sample with porosity 5.34% and permeability 0.1 mD, which is mainly composed of 20.5% quartz, 18.2% clay, 10% dolomite and 42.7% calcite, and the other is a tight sandstone with porosity 4.50% and permeability 0.28 mD, with 32% quartz, 29% soda feldspar, 12% k-feldspar and 20.3% clay minerals. For both the dry and fully water saturated conditions, these measurements were performed in a frequency range from 1 Hz to 1 kHz at room temperature by using the forced-oscillation method (Li et al., 2020; Spencer, 1981; Yin et al., 2017, 2019). The measured moduli dispersion of both samples apparently occurs in the whole measurement frequency band, and their porosities are measured by using a helium porosimeter (Li et al., 2020). In the experimental setup, the confining and pore pressures are set to 20 and 2 MPa, respectively. The bulk modulus, density and viscosity of water in the experiments are 2.25 GPa, 980 kg/m^3 and 0.001 Pa•s, respectively.

Microcracks and dissolved pores are observed in thin section of the tight-carbonate sample (see Figure 1b of Li et al., 2020), and these soft components with high compressibility are considered as inclusions (Borgomano et al., 2017). In contrast, the main matrix with intergranular pores can be treated as the host medium. According to Li et al. (2020), the dissolved pores with different sizes were observed in the thin section of the tight carbonate sample, in the range of 0.01–0.5 mm. Moreover, a larger crack of about 2 mm can be

Table 2
Properties of Tight Carbonate and Sandstone Samples

Samples	K_s (GPa)	K_{bH} (GPa)	K_{bI} (GPa)	ϕ_{H0} (%)	ϕ_{I0} (%)	κ_H mD	κ_I mD
Carbonate	72	62.6	6.8	4.82	10	0.09	0.9
Sandstone	31	20.9	0.6	4.33	10	0.27	5.7

observed in the thin section analysis. We slightly extend the range of the observed soft constituents, assuring that most potential inclusions can be incorporated. The range of the inclusion radii is set as (0.004–4) mm. The total inclusion volume, assumed to be 0.1, is associated with the volume ratio of the soft constituents containing microcracks and dissolved pores. The basic properties of the tight carbonate sample are given in Table 2.

A comparison between the measurements and predictions of the IPM model and Gassmann theory is shown in Figure 7. The results show that the estimated value of the Gassmann theory (the measured dry-rock bulk modulus $K_b = 38.44$ GPa is use in this theory) is smaller than the measured bulk modulus, which exceeds the experimental errors. This could mean that the Gassmann theory is not precise for low-porosity and low-permeability rocks. A possible explanation is that in the experiments, there is not enough time in a wave period for pore fluid pressure to equilibrate due to the low porosity and permeability of the carbonate sample. Another reason can be the presence of a chemical interaction between the frame and the fluid, which violates the hypothesis of the Gassmann theory (Mavko et al., 2009). To avoid the uncertainty of the laboratory measurements, we have to estimate the dry-rock elastic moduli from undrained measurements (at the low-frequency limit, where the saturated rock is relaxed) by using the inverse Gassmann Equation (Sun & Gurevich, 2020). The inverted dry-rock bulk (shear) modulus is 46.17 (25.12) GPa. With the values $D_f = 2.67$, $\theta = 0.02$, $r_0 = 10^{-3.8}$ and $\sigma_r{}^2 = 2$, the IPM model provides a good agreement with the

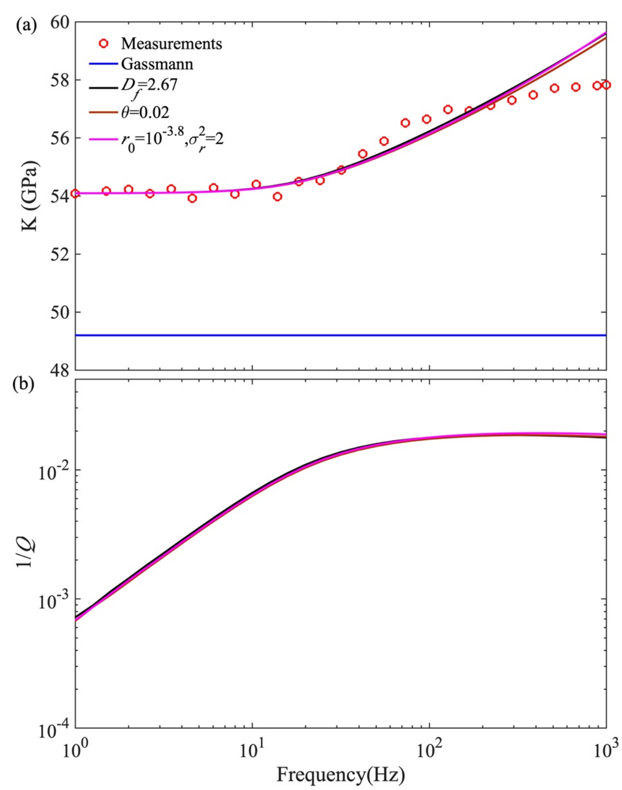

Figure 7. Experimental bulk modulus of the water-saturated tight carbonate (red circles) at a differential pressure of about 18 MPa, compared to the Gassmann prediction (blue line), and those of the self-similar (black line), exponential (brown line) and Gaussian (pink line) models.

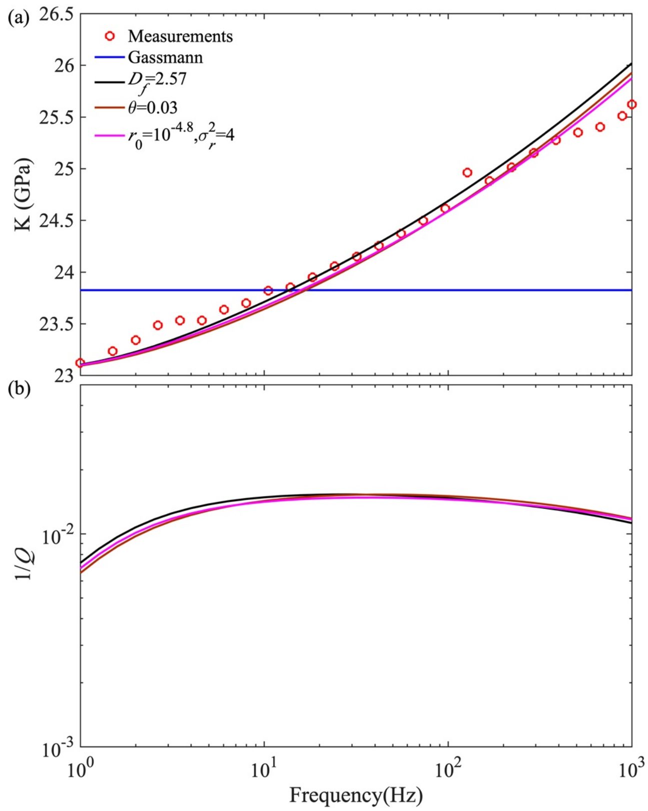

Figure 8. Experimental bulk modulus of the water-saturated tight sandstone (red circles) at a differential pressure of about 18 MPa, compared to the Gassmann predictions (blue line), and those of the self-similar (black line), exponential (brown line) and Gaussian (pink line) models.

measurements, where these values are obtained by a least-square regression. Note that the theoretical bulk modulus departs from the measured one at approximately 1 kHz. The reason of this difference may be that the inclusions in this sample are not characterized by the three distributions. Another reason is that the measured frequency range is relatively narrow, and there may be wave dispersion beyond this range (this behavior has been observed in measurements performed by Yin et al. [2017]). The attenuation is present at frequencies in the range 10 Hz–1 kHz (see Figure 7b).

For the sandstone sample, microcracks and grain contacts at different scales can be found in the thin section (see Figure 1a of Li et al., 2020), and these soft components are considered as inclusions. The total inclusion volume fraction is set as 0.03. The main matrix containing intergranular pores is considered as the host medium. The basic properties of the tight-sandstone sample are given in Table 2. Figure 8 compares the measurements with the predictions of the IPM theory and Gassmann theory. It is apparent that the measured bulk modulus monotonously increases with increasing frequency, implying that wave dispersion occurs in the whole (measured) frequency band. The Gassmann value is slightly higher than the measured value at 1 Hz, where the measured K_b is 18.99 GPa (this can be attributed to a weakening effect of the fluid on the grain contacts (Murphy et al., 1984), but the result is acceptable in view of the experimental errors of 3%–5%. The inverted bulk (shear) modulus from undrained measurements is 16.2 (5.26) GPa. Compared with the carbonate sample (Figure 7), the frequency range of anelasticity is broader, which implies that the scale range of the fabric structures (inclusions) in the sandstone is wider. Hence, this range is taken (0.001–10) mm. The predicted results of the IPM theory provide a better match with the measurements for $D_f = 2.57$, $\theta = 0.03$, $r_0 = 10^{-4.8}$ and $\sigma_r^2 = 4$, than those of the Gassmann theory. In addition, the predicted attenuation is stronger at frequencies of 1 Hz–1 kHz (see Figure 8b).

4.2. Laboratory Measurements for Fox Hills Sandstone

In this section, the IPM theory is applied to experimental data of Fox Hills sandstone with a porosity of 25.6% and a permeability of 9.48 mD. The matrix of the sample is dominated by quartz and clay minerals (mixture of kaolinite, chlorite, and smectite) (Bathija et al., 2009; Hasanov et al., 2019). Its elastic properties were measured by Batzle et al. (2006) from 5 to 800 Hz by using a forced deformation system and pulse transmission, where an extensional stress-strain measurement has been used to obtain low-frequency data (more details of the experimental procedure can be found in Batzle et al., 2006). The fluid used in the experiment is glycerine (63°C) with bulk modulus of 4.15 GPa, density of 1,235 kg/m^3 and viscosity of 0.0813 Pa•s (Yin et al., 2017). The inclusions are soft components composed by uncemented or loose-contact granular materials, and the host medium is a consolidated sandstone. The total inclusion volume fraction is 0.15. The basic properties of Fox Hills sandstone sample are listed in Table 3.

The comparison between measurements and predictions is illustrated in Figure 9. The results show that the experimental P-wave velocity at low frequencies is significantly less than that predicted by the Gassmann theory (the measured dry-rock bulk modulus K_b is 5.62 GPa). This behavior can also be observed in Figure 10a of Sun and Gurevich (2020). They showed that the measured bulk modulus at the pressure 3.5 MPa is significantly smaller than that estimated from the Gassmann theory at 3.5 MPa, and considered that the weakening of the saturated rock is related to the nonmechanical interaction with the glycerin. Hence the nonmechanical interaction between the rock frame and glycerin was considered

Table 3
Properties of Fox Hills Sandstone Sample

Samples	K_s (GPa)	K_{bH} (GPa)	K_{bI} (GPa)	ϕ_{H0} (%)	ϕ_{I0} (%)	κ_H mD	κ_I mD
Sandstone	37.2	6	0.4	25.4	27	8.2	82.1

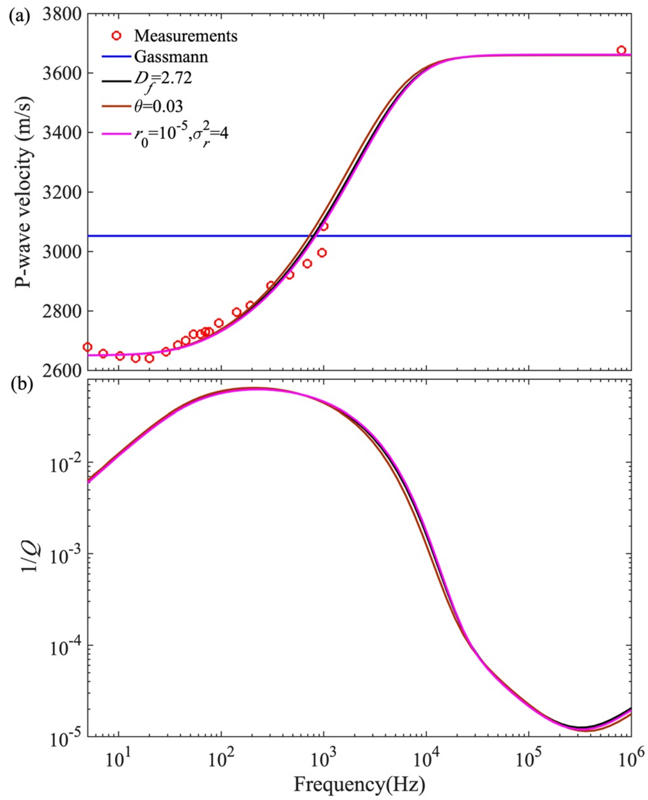

Figure 9. Experimental P-wave velocity of the glycerin-saturated Fox Hills sandstone (red circles) compared to the Gassmann prediction (blue line), and the self-similar (black line), the exponential (brown line) and the Gaussian (pink line) models.

to explain the discrepancy between the Gassmann's prediction and the data. The inverted dry-rock bulk (shear) modulus is 3.844 (1.256) GPa based on undrained measurements. By comparing Figure 7a with Figure 9a, it is shown that the measured dispersion is similar to that of the tight carbonate at seismic frequencies. In addition, Figure 9a shows that there is dispersion in the sonic band as well (10^3–10^5 Hz), which indicates that Fox Hills sandstone has a fabric structure (<0.004 mm) compared to the tight carbonate. The fabric structure scale is set in the range (0.002–2) mm. The IPM theory reasonably describes the P-wave velocity with $D_f = 2.72$, $\theta = 0.03$, $r_0 = 10^{-5}$ and ${\sigma_r}^2 = 4$.

4.3. Field Data for Marine Sediments

Marine sediments considered by Zhou et al. (2009) were collected at 20 different sites around the world and their sound speed and attenuation were measured in the frequency range of 50 Hz–400 kHz with different approaches (e.g., Gorgas et al., 2002; Potty et al., 2003; Thorsos et al., 2001). The P-wave velocity can be calculated as $V_P = R_a V_w$ (R_a is the sound speed ratio, and $V_w = 1{,}526$ m/s is the water sound speed), and the attenuation is $\alpha_s = (\pi f)/(Q V_P)$. The complexity of sedimentary environment causes a diversity of sediments, such as silt, sand-slit mixture, fine sand, medium sand and coarse sand. The grain bulk modulus is 32 GPa according to Zhao et al. (2009). The porosities and permeabilities changed from 0.36 to 0.47 and from 0.65×10^{-11} to 10×10^{-11} m^2, respectively. According to theoretical considerations and experiments (Isakson & Neilsen, 2006), soft sediments are composed of grain aggregates with different degrees of compaction, porosities higher than 0.5 and permeabilities higher than 10 D, embedded into consolidated sands, whose porosity and permeability are 0.395 and 8 D, respectively. The dry-rock bulk (shear) moduli of the host medium and inclusions are 0.5 (0.03) and 0.22 (0.028) GPa, respectively, whereas the total inclusion volume fraction is 0.0476. Figure 10 shows the P-wave velocity and attenuation compared with the

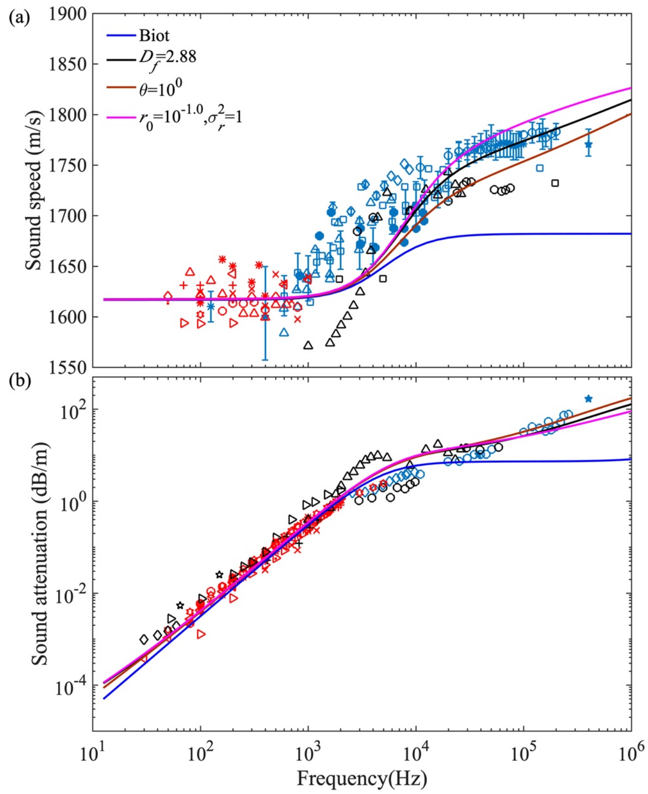

Figure 10. Full frequency-range measurements in sandy sea-bottoms, and predictions of the self-similar (black line), the exponential (brown line) and Gaussian (pink line) models. The symbols represent datasets from different authors (Zhou et al., 2009).

theoretical predictions. There is wave anelasticity in the full frequency range, and the Biot model cannot describe the measurements. When the scale range of the inclusion radius is (1.5–15,000) mm, the present model provides a better fit than the Biot theory for $D_f = 2.88$, $\theta = 1$, $r_0 = 0.1$ and $\sigma_r^2 = 1$. It can be inferred that a larger fabric structure (>1 mm) exists in the marine sediments.

5. Discussion

5.1. Adding Order of the Inclusion

In the classic DEM theory, the effective moduli of the composite medium are independent of the number of additions, when the addition number is sufficiently large. Similarly, the P-wave velocity and attenuation predicted from the IPM model approach the same values at the low- and high-frequency limits, with increasing number of inclusion additions. In contrast, the effective moduli depend on the order in which pores and cracks are added into the host (Han et al., 2016; Mavko et al., 2009; Tran et al., 2008). Hence, the order of inclusion addition affects the modeling results. To analyze this effect, the self-similar porous medium is selected as an example, where D_f is 2.77 and the scale of inclusion radii is in range (0.001–10) mm. The other properties are given in Table 1. By adding the inclusions from the small to large and randomly, the P-wave velocity and attenuation as a function of frequency are shown in Figure 11. The velocities are almost the same, while the attenuation curves are significantly different in the range 10^3–10^8 Hz, which is because the anelasticity effect at each step/addition depends on the order of addition. The wave-velocity dispersion is an integral/accumulative result of the velocity dispersion of previous additions, but it is less dependent on the order. On the other hand, the attenuation mainly reflects the anelasticity due to a single addition, not the accumulative effect, and is more dependent on the order. In this study, the inclusions are added into the host medium from small to large, according to the scales of the elastic wave observations, and a similar approach

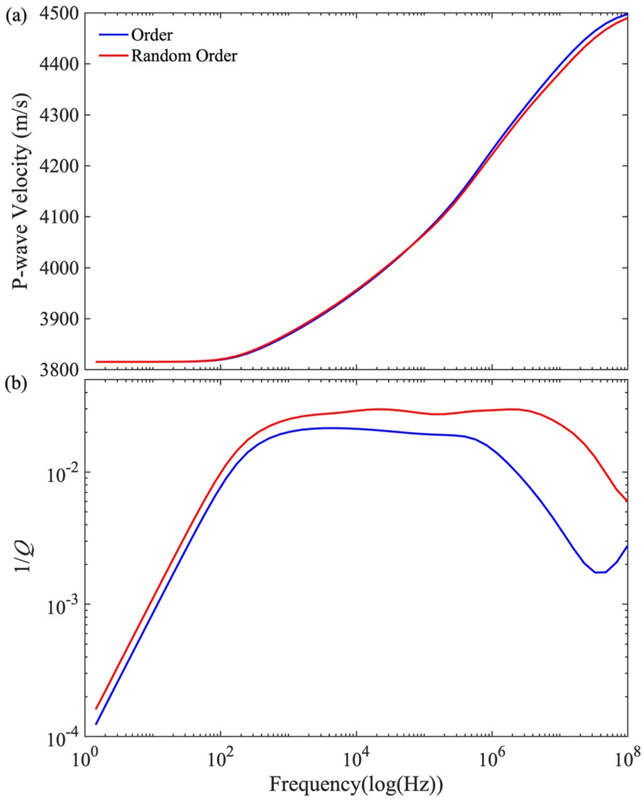

Figure 11. (a) P-wave velocity and (b) attenuation as a function of frequency, by adding the inclusions from the small to larger (blue line) and randomly (red line).

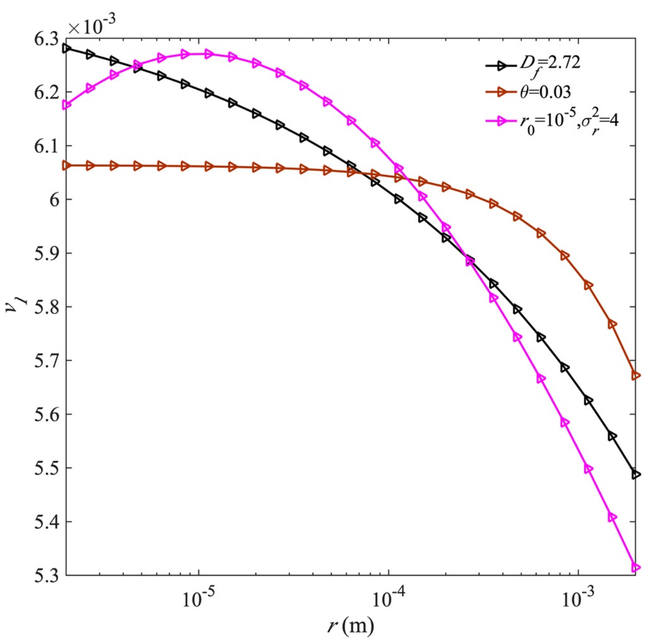

Figure 12. Volume fractions of the inclusions as a function of inclusion radius, with $D_f = 2.72$, $\theta = 0.03$, $r_0 = 10^{-5}$ and$\sigma_r^{\ 2} = 4$.

can be found in Bailly et al. (2019), who incrementally added pores (plug scale), cracks (outcrop scale) and fractures (seismic scale) into the host.

5.2. Assessment of the Modeling Result

The present theory gives the description for the measurements in laboratory and field experiments, and there is a discrepancy in Figures 7–9, that is, the results at low frequencies are not consistent with the Gassmann theory by using the measured bulk modulus. The reason can be a chemical or non-mechanical interaction between the rock frame and the fluid. In particular, if the saturating fluid is highly viscous, such as glycerin or heavy oil, their bulk modulus depends on frequency. The values of the fractal dimension D_f of this study are in agreement with the reported results for sandstones (2.55–2.89) and carbonates (2.27–2.75) (Krohn, 1988). To further analyze the coherence of the model, the volume fractions of the inclusions as a function of inclusion radius is given in Figure 12. Compared with Figure 9, there is a small difference between the results of the self-similar, exponential and Gaussian distributions, while the fractions of inclusions at the same radius are different. It is shown that different distributions may lead to the same wave anelasticity.

Similar to what was discussed in Ba et al. (2011), the proposed model analyzes the effects of local fluid flow at different scales induced by compressional waves, which causes significant P-wave dispersion and attenuation, but the S-wave dispersion mechanism is not incorporated here. The local fluid flow induced by S waves is different from that induced by P waves (Quintal et al., 2012), and their effects will be treated in a future study.

6. Conclusions

A theory of wave propagation in an infinituple-porosity media (IPM) is presented for the scale-dependent fabric structures, based on a DEM theory, where the governing Equations are derived from Hamilton's principle. The fabric or texture sizes are characterized by the exponential, Gaussian and self-similar distributions and the results show that broadband dispersion and attenuation are mainly related to the parameter θ, variance $\sigma_r^{\ 2}$ and fractal dimension D_f, respectively. Comparison with experimental laboratory data with different porosities and marine sediments gives a reasonable agreement. The modeling with the IPM theory yields different fabric scales, for example, (0.004–4) mm for a tight carbonate, (0.001–10) mm for a tight sandstone, (0.002–2) mm for Fox Hills sandstone and (1.5–15,000) mm for marine sediments. The theory provides an effective approach to describe the anelasticity of rocks with fabric structures at different scales and is helpful for gaining new insights into interpreting the observed broadband wave anelasticity in laboratory and field data. The IPM model proposed in this work can be validated against a serial of systematic numerical simulations by the numerical modeling approaches (e.g., Quintal et al., 2011; Wenzlau & Müller, 2009), which is highly valuable and should be considered in a future study.

Data Availability Statement

The measured data can be found in Li et al. (2020), Batzle et al. (2006), and Zhou et al. (2009), and the data of the modeling results of the three distributions in: https://zenodo.org/record/4147112#.X5ljU3gzZ24.

Acknowledgments
The authors are grateful to the support of the Jiangsu Innovation and Entrepreneurship Plan, Jiangsu Province Science Fund for Distinguished Young Scholars and National Natural Science Foundation of China (41974123). The authors are grateful to Dr. Li Hui for the helpful discussions.

References

Ba, J., Carcione, J. M., Cao, H., Du, Q. Z., Yuan, Z. Y., & Lu, M. H. (2012). Velocity dispersion and attenuation of P waves in partially-saturated rocks: Wave propagation Equations in double-porosity medium. *Chinese Journal of Geophysics*, *55*(1), 219–231. https://doi.org/10.6038/j.issn.0001-5733.2012.01.021

Ba, J., Carcione, J. M., & Nie, J. X. (2011). Biot-Rayleigh theory of wave propagation in double-porosity media. *Journal of Geophysical Research*, *116*, B06202. https://doi.org/10.1029/2010JB008185

Ba, J., Carcione, J. M., & Sun, W. (2015). Seismic attenuation due to heterogeneities of rock fabric and fluid distribution. *Geophysical Journal International*, *202*(3), 1843–1847. https://doi.org/10.1093/gji/ggv255

Ba, J., Xu, W., Fu, L. Y., Carcione, J. M., & Zhang, L. (2017). Rock anelasticity due to patchy saturation and fabric heterogeneity: A double double-porosity model of wave propagation. *Journal of Geophysical Research: Solid Earth*, *122*, 1949–1976. https://doi.org/10.1002/2016JB013882

Bailly, C., Fortin, J., Adelinet, M., & Hamon, Y. (2019). Upscaling of elastic properties in carbonates: A modeling approach based on a multiscale geophysical data set. *Journal of Geophysical Research: Solid Earth*, *124*, 13021–13038. https://doi.org/10.1029/2019JB018391

Bathija, A. P., Batzle, M. L., & Prasad, M. (2009). An experimental study of the dilation factor. *Geophysics*, *74*(4), E181–E191. https://doi.org/10.1190/1.3137060

Batzle, M. L., Han, D. H., & Hofmann, R. (2006). Fluid mobility and frequency-dependent seismic velocity—Direct measurements. *Geophysics*, *71*(1), N1–N9. https://doi.org/10.1190/1.2159053

Benveniste, Y. (1987). A new approach to the application of Mori-Tanaka's theory in composite materials. *Mechanics of Materials*, *6*(2), 147–157. https://doi.org/10.1016/0167-6636(87)90005-6

Berryman, J. G. (1979). Theory of elastic properties of composite materials. *Applied Physics Letters*, *35*(11), 856–858. https://doi.org/10.1063/1.90982

Berryman, J. G. (1980a). Long-wavelength propagation in composite elastic media. I Spherical inclusions. *Journal of the Acoustical Society of America*, *68*, 1809–1819. https://doi.org/10.1121/1.385171

Berryman, J. G. (1980b). Long-wavelength propagation in composite elastic media. II Ellipsoidal inclusions. *Journal of the Acoustical Society of America*, *68*, 1820–1831. https://doi.org/10.1121/1.385172

Berryman, J. G. (1992). Single-scattering approximations for coefficients in Biot's Equations of poroelasticity. *Journal of the Acoustical Society of America*, *91*(2), 551–571. https://doi.org/10.1121/1.402518

Best, A. I., Priest, J. A., Clayton, C. R., & Rees, E. V. (2013). The effect of methane hydrate morphology and water saturation on seismic wave attenuation in sand under shallow sub-seafloor conditions. *Earth and Planetary Science Letters*, *368*, 78–87. https://doi.org/10.1016/j.epsl.2013.02.033

Biot, M. A. (1956). Theory of propagation of elastic waves in a fluid-saturated porous solid. II. Higher frequency range. *Journal of the Acoustical Society of America*, *28*(2), 179–191. https://doi.org/10.1121/1.1908241

Biot, M. A. (1962). Mechanics of deformation and acoustic propagation in porous media. *Journal of Applied Physics*, *33*(4), 1482–1498. https://doi.org/10.1063/1.1728759

Borgomano, J. V. M., Pimienta, L., Fortin, J., & Guéguen, Y. (2017). Dispersion and attenuation measurements of the elastic moduli of a dual-porosity limestone. *Journal of Geophysical Research: Solid Earth*, *122*, 2690–2711. https://doi.org/10.1002/2016JB013816

Carcione, J. M., Farina, B., Poletto, F., Qadrouh, A. N., & Cheng, W. (2020). Seismic attenuation in partially molten rocks. *Physics of the Earth and Planetary Interiors*. https://doi.org/10.1016/j.pepi.2020.106568

Carcione, J. M., & Gurevich, B. (2011). Differential form and numerical implementation of Biot's poroelasticity Equations with squirt dissipation. *Geophysics*, *76*(6), N55–N64. https://doi.org/10.1190/geo2010-0169.1

Carcione, J. M., Helle, H. B., & Pham, N. H. (2003). White's model for wave propagation in partially saturated rocks: Comparison with poroelastic numerical experiments. *Geophysics*, *68*, 1389–1398. https://doi.org/10.1190/1.1598132

Carcione, J. M., & Picotti, S. (2006). P-wave seismic attenuation by slow-wave diffusion. Effects of inhomogeneous rock properties. *Geophysics*, *71*, O1–O8. https://doi.org/10.1190/1.2194512

Chapman, M., Zatsepin, S. V., & Crampin, S. (2002). Derivation of a microstructural poroelastic model. *Geophysical Journal International*, *151*(2), 427–451. https://doi.org/10.1046/j.1365-246X.2002.01769.x

David, E. C., & Zimmerman, R. W. (2011). Compressibility and shear compliance of spheroidal pores: Exact derivation via the Eshelby tensor, and asymptotic expressions in limiting cases. *International Journal of Solids and Structures*, *48*(5), 680–686. https://doi.org/10.1016/j.ijsolstr.2010.11.001

David, E. C., & Zimmerman, R. W. (2012). Pore structure model for elastic wave velocities in fluid-saturated sandstones. *Journal of Geophysical Research*, *117*, B07210. https://doi.org/10.1029/2012JB009195

Dvorkin, J., & Nur, A. (1993). Dynamic poroelasticity: A unified model with the squirt and the Biot mechanisms. *Geophysics*, *58*(4), 524–533. https://doi.org/10.1190/1.1443435

Eshelby, J. D. (1957). The determination of the elastic field of an ellipsoidal inclusion, and related problems. *Proceedings of the Royal Society of London. Series A. Mathematical and Physical Sciences*, *241*(1226), 376–396. https://doi.org/10.1098/rspa.1957.0133

Gassmann, F. (1951). Über die elastizität poröser medien: Vier. der Natur. *Gesellschaft Zürich*, *96*, 1–23.

Gist, G. A. (1994). Interpreting laboratory velocity measurements in partially gas-saturated rocks. *Geophysics*, *59*(7), 1100–1109. https://doi.org/10.1190/1.1443666

Glubokovskikh, S., Gurevich, B., & Saxena, N. (2016). A dual-porosity scheme for fluid/solid substitution. *Geophysical Prospecting*, *64*, 1112–1121. https://doi.org/10.1111/1365-2478.12389

Gorgas, T. J., Wilkens, R. H., Fu, S. S., Frazer, L. N., Richardson, M. D., Briggs, K. B., & Lee, H. (2002). In situ acoustic and laboratory ultrasonic sound speed and attenuation measured in heterogeneous soft seabed sediments: Eel River shelf, California. *Marine Geology*, *182*(1–2), 103–119. https://doi.org/10.1016/S0025-3227(01)00230-4

Guo, J., & Gurevich, B. (2020a). Frequency-dependent P wave anisotropy due to wave-induced fluid flow and elastic scattering in a fluid-saturated porous medium with aligned fractures. *Journal of Geophysical Research: Solid Earth*, *125*, e2020JB020320. https://doi.org/10.1029/2020JB020320

Guo, J., & Gurevich, B. (2020b). Effects of coupling between wave-induced fluid flow and elastic scattering on P-wave dispersion and attenuation in rocks with aligned fractures. *Journal of Geophysical Research: Solid Earth*, *125*, e2019JB018685. https://doi.org/10.1029/2019JB018685

Gurevich, B., Makarynska, D., de Paula, O. B., & Pervukhina, M. (2010). A simple model for squirt-flow dispersion and attenuation in fluid-saturated granular rocks. *Geophysics*, *75*(6), N109–N120. https://doi.org/10.1190/1.3509782

Han, T. (2016). A simple way to model the pressure dependency of rock velocity. *Tectonophysics*, *675*, 1–6. https://doi.org/10.1016/j.tecto.2016.03.008

Hasanov, A. K., Dugan, B., Batzle, M. L., & Prasad, M. (2019). Hydraulic and poroelastic rock properties from oscillating pore pressure experiments. *Journal of Geophysical Research: Solid Earth*, *124*, 4473–4491. https://doi.org/10.1029/2018JB017276

Ikelle, L. T., Yung, S. K., & Daube, F. (1993). 2-D random media with ellipsoidal autocorrelation functions. *Geophysics*, *58*(9), 1359–1372. https://doi.org/10.1190/1.1443518

Isakson, M. J., & Neilsen, T. B. (2006). The viability of reflection loss measurement inversion to predict broadband acoustic behavior. *Journal of the Acoustical Society of America*, *120*(1), 135–144. https://doi.org/10.1121/1.2206515

Jakobsen, M., Hudson, J. A., & Hansen, A. (2003). T-matrix approach to shale acoustics. *Geophysical Journal International*, *154*, 533–558. https://doi.org/10.1046/j.1365-246X.2003.01977.x

Katz, A., & Thompson, A. H. (1985). Fractal sandstone pores: Implications for conductivity and pore formation. *Physical Review Letters*, *54*(12), 1325. https://doi.org/10.1103/PhysRevLett.54.1325

King, M. S., & Marsden, J. R. (2002). Velocity dispersion between ultrasonic and seismic frequencies in brine-saturated reservoir sandstones. *Geophysics*, *67*(1), 254–258. https://doi.org/10.1190/1.1451700

Klimeš, L. (2002). Correlation functions of random media. *Pure and Applied Geophysics*, *159*(7–8), 1811–1831. https://doi.org/10.1007/s00024-002-8710-2

Krohn, C. E. (1988). Sandstone fractal and Euclidean pore volume distributions. *Journal of Geophysical Research*, *93*(B4), 3286–3296. https://doi.org/10.1029/JB093iB04p03286

Kuster, G. T., & Toksöz, M. N. (1974). Velocity and attenuation of seismic waves in two-phase media: Part I. Theoretical formulations. *Geophysics*, *39*(5), 587–606. https://doi.org/10.1190/1.1440450

Li, H., Wang, D., Gao, J., Zhang, M., Wang, Y., Zhao, L., & Yang, Z. (2020). Role of saturation on elastic dispersion and attenuation of tight rocks: An experimental study. *Journal of Geophysical Research: Solid Earth*, *125*, e2019JB018513. https://doi.org/10.1029/2019JB018513

Liu, J., Ma, J. W., & Yang, H. Z. (2009). Research on dispersion and attenuation of P wave in periodic layered-model with patchy saturation. *Chinese Journal of Geophysics*, *52*(11), 2879–2885. https://doi.org/10.3969/j.issn.0001-5733.2009.11.023

Liu, J., Ma, J. W., & Yang, H. Z. (2010). Research on P-wave's propagation in White's sphere model with patchy saturation. *Chinese Journal of Geophysics, 53*(4), 954–962.

Matonti, C., Guglielmi, Y., Viseur, S., Bruna, P. O., Borgomano, J., Dahl, C., & Marié, L. (2015). Heterogeneities and diagenetic control on the spatial distribution of carbonate rocks acoustic properties at the outcrop scale. *Tectonophysics*, *638*, 94–111. https://doi.org/10.1016/j.tecto.2014.10.020

Mavko, G., & Jizba, D. (1991). Estimating grain-scale fluid effects on velocity dispersion in rocks. *Geophysics*, *56*(12), 1940–1949. https://doi.org/10.1190/1.1443005

Mavko, G., Mukerji, T., & Dvorkin, J. (2009). *The rock Physics Handbook*. Cambridge University Press.

Mavko, G., & Nur, A. (1975). Melt squirt in the asthenosphere. *Journal of Geophysical Research*, *80*(11), 1444–1448. https://doi.org/10.1029/JB080i011p01444

Mori, T., & Tanaka, K. (1973). Average stress in matrix and average elastic energy of materials with misfitting inclusions. *Acta Metallurgica*, *21*(5), 571–574. https://doi.org/10.1016/0001-6160(73)90064-3

Müller, T. M., & Gurevich, B. (2005). Wave-induced fluid flow in random porous media: Attenuation and dispersion of elastic waves. *Journal of the Acoustical Society of America*, *117*(5), 2732–2741. https://doi.org/10.1121/1.1894792

Müller, T. M., Gurevich, B., & Lebedev, M. (2010). Seismic wave attenuation and dispersion resulting from wave-induced flow in porous rocks—A review. *Geophysics*, *75*, 75A147–75A164. https://doi.org/10.1190/1.3463417

Müller, T. M., Toms-Stewart, J., & Wenzlau, F. (2008). Velocity-saturation relation for partially saturated rocks with fractal pore fluid distribution. *Geophysical Research Letters*, *35*, L09306. https://doi.org/10.1029/2007GL033074

Murphy, W. F., III, Winkler, K. W., & Kleinberg, R. L. (1984). Frame modulus reduction in sedimentary rocks: The effect of adsorption on grain contacts. *Geophysical Research Letters*, *11*(9), 805–808. https://doi.org/10.1029/GL011i009p00805

Norris, A. N. (1985). A differential scheme for the effective moduli of composites. *Mechanics of Materials*, *4*(1), 1–16. https://doi.org/10.1016/0167-6636(85)90002-X

Pimienta, L., Fortin, J., & Guéguen, Y. (2015a). Bulk modulus dispersion and attenuation in sandstones. *Geophysics*, *80*(2), D111–D127. https://doi.org/10.1190/geo2014-0335.1

Pimienta, L., Fortin, J., & Guéguen, Y. (2015b). Experimental study of Young's modulus dispersion and attenuation in fully saturated sandstones. *Geophysics*, *80*, L57–L72. https://doi.org/10.1190/geo2014-0532.1

Potty, G. R., Miller, J. H., & Lynch, J. F. (2003). Inversion for sediment geoacoustic properties at the New England Bight. *Journal of the Acoustical Society of America*, *114*(4), 1874–1887. https://doi.org/10.1121/1.1605391

Pride, S. R., Berryman, J. G., & Harris, J. M. (2004). Seismic attenuation due to wave-induced flow. *Journal of Geophysical Research*, *109*, B01201. https://doi.org/10.1029/2003JB002639

Pride, S. R., & Masson, Y. J. (2006). Acoustic attenuation in self-affine porous structures. *Physical Review Letters*, *97*(18), 184301. https://doi.org/10.1103/PhysRevLett.97.184301

Quintal, B., Steeb, H., Frehner, M., & Schmalholz, S. M. (2011). Quasi-static finite element modeling of seismic attenuation and dispersion due to wave-induced fluid flow in poroelastic media. *Journal of Geophysical Research*, *116*, B01201. https://doi.org/10.1029/2010JB007475

Quintal, B., Steeb, H., Frehner, M., Schmalholz, S. M., & Saenger, E. H. (2012). Pore fluid effects on S-wave attenuation caused by wave-induced fluid flow. *Geophysics*, *77*(3), L13–L23. https://doi.org/10.1190/geo2011-0233.1

Rao, Y., Fu, L. Y., Wu, Y., & Boateng, C. D. (2020). Heterogeneous characteristic analysis of shale based on multi-component and multi-scale random media method. *Chinese Journal of Geophysics*, *63*(7), 2800–2809. https://doi.org/10.6038/cjg2020N0062

Rieu, M., & Perrier, E. (1998). Fractal models of fragmented and aggregated soils. In B. Philippe, P. Jean-Yves, & A. S. Bobby (Eds.), *Fractals in soil science advances in Soil Science. Fractals in Soil Science* (pp. 169–202). Boca Raton, FL: CRC Press.

Santos, J. E., & Carcione, J. M. (2015). Finite-element harmonic experiments to model fractured induced anisotropy in poroelastic media. *Computer Methods in Applied Mechanics and Engineering*, *283*, 1189–1213. https://doi.org/10.1016/j.cma.2014.08.016

Sarout, J. (2012). Impact of pore space topology on permeability, cut-off frequencies and validity of wave propagation theories. *Geophysical Journal International*, *189*(1), 481–492. https://doi.org/10.1111/j.1365-246X.2011.05329.x

Sun, W., Ba, J., & Carcione, J. M. (2016). Theory of wave propagation in partially saturated double-porosity rocks: A triple-layer patchy model. *Geophysical Supplements to the Monthly Notices of the Royal Astronomical Society*, *205*(1), 22–37. https://doi.org/10.1093/gji/ggv551

Sun, W., Xiong, F., Ba, J., & Carcione, J. M. (2018). Effects of ellipsoidal heterogeneities on wave propagation in partially saturated double-porosity rocks. *Geophysics*, *83*(3), WC71–WC81. https://doi.org/10.1190/geo2017-0549.1

Sun, Y., & Gurevich, B. (2020). Modeling the effect of pressure on the moduli dispersion in fluid-saturated rocks. *Journal of Geophysical Research: Solid Earth*, *125*, e2019JB019297. https://doi.org/10.1029/2019JB019297

Tang, X. (2011). A unified theory for elastic wave propagation through porous media containing cracks—An extension of Biot's poroelastic wave theory. *Science China Earth Sciences*, *54*(9), 1441. https://doi.org/10.1007/s11430-011-4245-7

Tang, X. M., Chen, X. L., & Xu, X. K. (2012). A cracked porous medium elastic wave theory and its application to interpreting acoustic data from tight formations. *Geophysics*, *77*(6), D245–D252. https://doi.org/10.1190/geo2012-0091.1

Thorsos, E. I., Williams, K. L., Chotiros, N. P., Christoff, J. T., Commander, K. W., Greenlaw, C. F., & Tang, D. (2001). An overview of SAX99: Acoustic measurements. *IEEE Journal of Oceanic Engineering*, *26*(1), 4–25. https://doi.org/10.1109/48.917916

Tisato, N., & Quintal, B. (2013). Measurements of seismic attenuation and transient fluid pressure in partially saturated Berea sandstone: Evidence of fluid flow on the mesoscopic scale. *Geophysical Journal International*, *195*(1), 342–351. https://doi.org/10.1093/gji/ggt259

Tran, D. T., Rai, C. S., & Sondergeld, C. H. (2008). Changes in crack aspect-ratio concentration from heat treatment: A comparison between velocity inversion and experimental data. *Geophysics*, *73*(4), E123–E132. https://doi.org/10.1190/1.2928848

Walsh, J. B. (1965). The effect of cracks on the compressibility of rock. *Journal of Geophysical Research*, *70*(2), 381–389. https://doi.org/10.1029/JZ070i002p00381

Wenzlau, F., & Müller, T. M. (2009). Finite-difference modeling of wave propagation and diffusion in poroelastic media. *Geophysics*, *74*(4), T55–T66. https://doi.org/10.1190/1.3122928

White, J. E. (1975). Computed seismic speeds and attenuation in rocks with partial gas saturation. *Geophysics*, *40*(2), 224–232. https://doi.org/10.1190/1.1440520

White, J. E., Mihailova, N., & Lyakhovitsky, F. (1975). Low-frequency seismic waves in fluid-saturated layered rocks. *Journal of the Acoustical Society of America*, *57*(S1), S30. https://doi.org/10.1121/1.1995164

Wu, C., Ba, J., Carcione, J. M., Fu, L. Y., Chesnokov, E. M., & Zhang, L. (2020). A squirt-flow theory to model wave anelasticity in rocks containing compliant microfractures. *Physics of the Earth and Planetary Interiors*, *301*, 106450. https://doi.org/10.1016/j.pepi.2020.106450

Wu, T. T. (1966). The effect of inclusion shape on the elastic moduli of a two-phase material. *International Journal of Solids and Structures*, *2*, 1–8. https://doi.org/10.1016/0020-7683(66)90002-3

Yao, Q., Han, D. H., Yan, F., & Zhao, L. (2015). Modeling attenuation and dispersion in porous heterogeneous rocks with dynamic fluid modulus. *Geophysics*, *80*(3), D183–D194. https://doi.org/10.1190/geo2013-0410.1

Yin, H., Borgomano, J. V., Wang, S., Tiennot, M., Fortin, J., & Guéguen, Y. (2019). Fluid substitution and shear weakening in clay-bearing sandstone at seismic frequencies. *Journal of Geophysical Research: Solid Earth*, *124*, 1254–1272. https://doi.org/10.1029/2018JB016241

Yin, H., Zhao, J., Tang, G., Zhao, L., Ma, X., & Wang, S. (2017). Pressure and fluid effect on frequency-dependent elastic moduli in fully saturated tight sandstone. *Journal of Geophysical Research: Solid Earth*, *122*, 8925–8942. https://doi.org/10.1002/2017JB014244

Zhang, B., Yang, D., Cheng, Y., & Zhang, Y. (2019). A unified poroviscoelastic model with mesoscopic and microscopic heterogeneities. *Science Bulletin*, *64*(17), 1246–1254. https://doi.org/10.1016/j.scib.2019.05.027

Zhang, L., Ba, J., Carcione, J. M., & Fu, L. Y. (2020). Differential poroelasticity model for wave dissipation in self-similar rocks. *International Journal of Rock Mechanics and Mining Sciences*, *128*, 104281. https://doi.org/10.1016/j.ijrmms.2020.104281

Zhang, L., Ba, J., Carcione, J. M., & Sun, W. (2019). Modeling wave propagation in cracked porous media with penny-shaped inclusions. *Geophysics*, *84*, WA141–WA151. https://doi.org/10.1190/geo2018-0487.1

Zhao, L., Cao, C., Yao, Q., Wang, Y., Li, H., Yuan, H., & Han, D. H. (2020). Gassmann Consistency for Different Inclusion-Based Effective Medium Theories: Implications for Elastic Interactions and Poroelasticity. *Journal of Geophysical Research: Solid Earth*, *125*, e2019JB018328. https://doi.org/10.1029/2019JB018328

Zheng, P., Ding, B., & Sun, X. (2017). Elastic wave attenuation and dispersion induced by mesoscopic flow in double-porosity rocks. *International Journal of Rock Mechanics and Mining Sciences*, *91*, 104–111. https://doi.org/10.1016/j.ijrmms.2016.11.018

Zhou, J. X., Zhang, X. Z., & Knobles, D. P. (2009). Low-frequency geoacoustic model for the effective properties of sandy seabottoms. *Journal of the Acoustical Society of America*, *125*(5), 2847–2866. https://doi.org/10.1121/1.3089218

Zimmerman, R. W. (1991). Elastic moduli of a solid containing spherical inclusions. *Mechanics of Materials*, *12*, 17–24. https://doi.org/10.1016/0167-6636(91)90049-6